Journal of Materials Chemistry A

PAPER

View Article Online
View Journal | View Issue

Cite this: J. Mater. Chem. A, 2015, 3, 8545

Core–shell structured $Li_{0.33}La_{0.56}TiO_3$ perovskite as a highly efficient and sulfur-tolerant anode for solid-oxide fuel cells†

Wei Wang,[ab] Jifa Qu,[a] Bote Zhao,[a] Guangming Yang[a] and Zongping Shao*[ab]

Received 13th February 2015
Accepted 16th March 2015

DOI: 10.1039/c5ta01213a

www.rsc.org/MaterialsA

Solid oxide fuel cells (SOFCs), which directly convert chemical energy into electricity, have several advantages, such as fuel flexibility and low emissions. Unfortunately, the performance and stability of SOFCs with state-of-the-art Ni-based anodes are sensitive to impurities, such as sulfur, which is a common component of practical fuels, including natural gas and renewable biogas. The development of sulfur-tolerant anode materials is important for successfully operating SOFCs with sulfur-containing practical fuels. In this study, a core–shell architecture was fabricated from solution infiltration and was evaluated as a sulfur-tolerant anode for SOFCs. For the first time, we used a lithium conductive material, $Li_{0.33}La_{0.56}TiO_3$ (LLTO, perovskite oxide), as the shell for anodic reactions. The resulting cell delivered higher electrochemical activities than similar cells, with widely used sulfur-tolerant perovskite anodes. In addition, the cell with the core–shell structured anode demonstrated favorable stability over 70 hours' operation when using 1000 ppm H_2S–H_2 fuel at 800 °C. In contrast, the cell with an anode composed of nanoparticles failed after only 5.5 hours under the same operation conditions. This study offers a new strategy for developing highly sulfur tolerant and efficient anodes for SOFCs.

Introduction

Over 40 megatons of hydrogen sulfide (H_2S) are produced every year worldwide as by-products from petroleum, natural gas and coal gasification industries.[1,2] Due to the negative effects of H_2S on the environment, equipment and human health, its disposal and treatment are considered a worldwide problem. There are few direct commercial uses for H_2S, and most H_2S is converted to sulfur in the two-step Claus process.[3] However, these reactions are highly exothermic. During the H_2S disposal process, only part of the energy can be recovered as low-grade energy during the production of steam, while the other part is wasted.

As a new type of high-temperature energy-conversion device with high efficiency, fuel flexibility and high-quality exhaust heat, solid oxide fuel cells (SOFCs) should provide a useful solution for removing H_2S.[4–8] Pujare *et al.* first proposed a SOFC for successfully removing H_2S in 1987.[9] A key technical challenge in the development of H_2S integrated SOFC systems is to identify anode materials that are conductive, chemically and electrochemically stable and catalytically active in H_2S-containing environments. The most commonly used anodes for SOFCs are Ni-based cermets, which contain metallic Ni and an ion-conducting electrolyte material, such as yttrium-stabilized ZrO_2 (YSZ). However, Ni-based anodes suffer from serious poisoning, even though a very low H_2S content (<10 ppm) exists in the fuel, although they are excellent anodes for an SOFC operated on hydrogen.[10–12] In contrast, the natural gas and biogas had much higher H_2S contents, and the direct utilization of these fuels in SOFCs could effectively reduce operation costs.[13,14] Therefore, designing anode materials that can be operated on fuels containing larger H_2S concentrations is important for commercializing SOFCs. Many perovskite oxides, such as $La_{0.75}Sr_{0.25}Cr_{0.5}Mn_{0.5}O_{3-\delta}$, $La_{0.7}Sr_{0.3}VO_3$, $Sr_2Mg_{1-x}Mn_xMoO_{6-\delta}$ and $BaZr_{0.1}Ce_{0.7}Y_{0.2-x}Yb_xO_{3-\delta}$, have been examined as sulfur-tolerant anode materials.[15–21] Among them, $SrTiO_3$, $BaTiO_3$ and $La_2Ti_2O_7$ as well as the substituted Ti-based perovskites are very attractive and reliable alternative anode materials for SOFCs because they have a high sulfur tolerance.[22–25] However, the power outputs of cells with these anodes remain low, and the stabilities of their phase structures under operation conditions are not sufficient. Consequently, substantial progress must be made to develop perovskite-type anode materials with improved activity and stability.

Infiltration techniques have been widely applied in the preparation of perovskite anode materials. According to the different firing temperatures, the nanostructure of the infiltrated anode can be divided into two aspects: discrete particles and a continuous and conformal thin film. However, sulfur poisoning could result in the agglomeration of perovskite oxide

[a]State Key Laboratory of Materials-Oriented Chemical Engineering, College of Chemistry & Chemical Engineering, Nanjing Tech University, No. 5 Xin Mofan Road, Nanjing 210009, P. R. China. E-mail: shaozp@njtech.edu.cn

[b]Department of Chemical Engineering, Curtin University, Perth, WA 6845, Australia

† Electronic supplementary information (ESI) available. See DOI: 10.1039/c5ta01213a

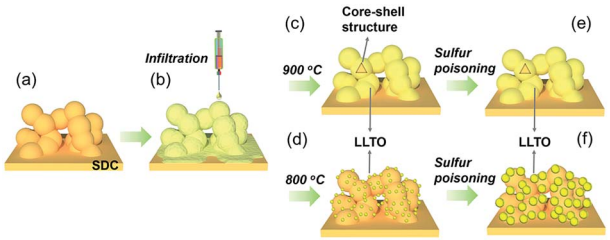

Fig. 1 Schematic diagrams of the preparation processes for the nanoparticle-decorated electrode and core–shell structured electrode prepared by solution infiltration (a–d) and the possible mechanism for the sulfur poisoning process of the different anodes (e and f).

nanoparticles. Thin films or core–shell structures are thermally more stable than nanoparticles and can avoid further sintering and thermomechanical stress.[26,27] Therefore, the development of an active and stable core–shell structured electrode to battle the sulfur poisoning problem is important.

Herein, we propose an innovative anode consisting of an active shell ($Li_{0.33}La_{0.56}TiO_3$, LLTO) coated on a porous stable core ($Sm_{0.2}Ce_{0.8}O_{1.9}$, SDC) for applications in SOFCs operating on H_2S-containing fuels. The LLTO shows high lithium-ion conductivity. Thus, the lithium in the bulk could compensate for a loss in surface lithium due to evaporation at elevated temperatures, making LLTO very stable in its phase structure. The shell was fabricated using a simple solution infiltration method. The resulting anode exhibited excellent sulfur tolerance, high hydrogen electrochemical activity and superior durability at intermediate temperatures. These findings could provide a new strategy for designing active and stable anodes for SOFCs.

The formation process of the core–shell structured electrode and a possible mechanism for improving sulfur tolerance were proposed, as shown in Fig. 1. Infiltration processes involve two successive steps: (i) the preparation of a porous electrode backbone (Fig. 1a), and (ii) infiltration of an electro-active phase. The backbone was fired at 1200 °C to obtain excellent bonding with the electrolyte, excellent connectivity for effective electron and oxygen ion conduction, and good structural stability under operating conditions. A liquid solution containing metal salt precursors, favorable surfactants and complex agents was introduced into the backbone (Fig. 1b). After subsequent thermal treatment, two typical morphologies can be observed: discrete particles (Fig. 1c) and a continuous and conformal thin film (Fig. 1d). In addition, the core–shell-structured electrode effectively improved the thermal stability by avoiding further sintering due to sulfur poisoning (Fig. 1e). As shown in Fig. 1f, serious agglomeration of the LLTO nanoparticles is expected during the sulfur poisoning process. Consequently, excellent operational stability is achieved when using the core–shell-structured anode.

Results and discussion

First, we used a scanning electron microscope (SEM) to study the morphology of the infiltrated anodes. An SEM image of the as-prepared SDC scaffold is shown in Fig. 2a. This image demonstrates a highly porous morphological structure that is loaded with well-distributed nanoparticles and has a porosity of approximately 50%. Fig. 2b to d show SEM images of the LLTO-infiltrated SDC anodes after firing at 800, 900 and 1000 °C, respectively. For the infiltrated anode calcined at 800 °C, clusters of nanoparticles with diameters of ~50 nm were clearly observed on the surface of the SDC scaffold (Fig. 2b). The nanoparticles disappeared after calcination at 900 °C, indicating the formation of a LLTO thin film over the SDC scaffold. However, after calcination at 1000 °C, the anode was seriously sintered, as shown by the sharp decrease in the porosity of the anode (Fig. 2d).

To understand the formation of a LLTO thin film over the SDC scaffold surface after firing at 900 °C, the fired anode particles were characterized using transmission electron microscopy (TEM). As shown in Fig. 3, a core (darker area) and a shell (brighter area) with a thickness of less than 50 nm were observed on the LLTO infiltrated electrodes. A lattice space of 0.273 nm was detected from the outermost portion, which corresponded to the (110) diffraction plane of the LLTO phase. To further clarify the chemical composition of the core–shell particles, energy dispersive X-ray (EDX) was performed. The resulting data are listed in Table 1. According to the atomic distribution of core–shell particles from three different samples, the atomic contents of Sm and Ce were dominant in the darker areas, and the contents of Ti and La were much higher in the brighter area. Therefore, the darker areas can be regarded as the SDC-rich regions, and the brighter areas (outer layer) can be considered as the LLTO-rich regions. In combination with the SEM images shown in Fig. 2, it is reasonable to deduce that the core–shell structured anode is formed after high temperature firing (above 900 °C).

To obtain information regarding the phase composition of the infiltrated anodes, X-Ray Diffraction (XRD) characterization was performed (as shown in Fig. 4a). For comparison, the XRD

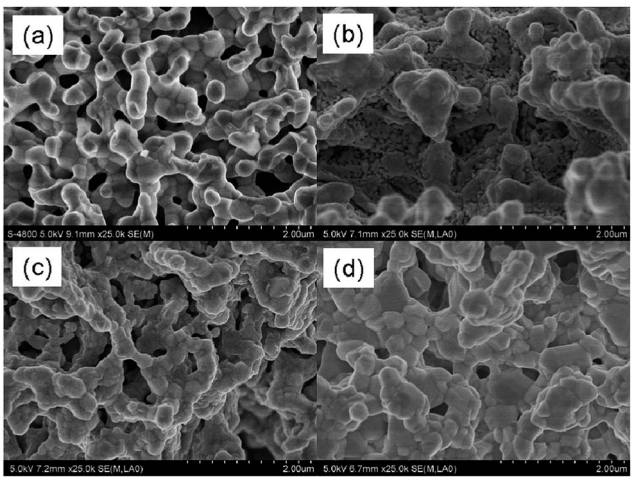

Fig. 2 SEM images of (a) as-prepared SDC scaffold and the LLTO-infiltrated SDC anodes after firing at (b) 800, (c) 900 and (d) 1000 °C for 2 hours.

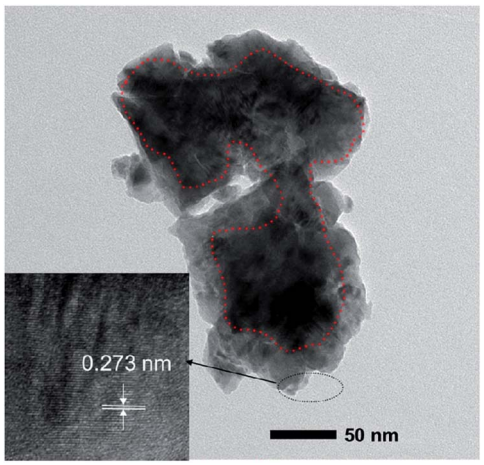

Fig. 3 TEM results under different magnifications of the core–shell structured LLTO-infiltrated SDC anodes.

Table 1 Atomic distribution (%) of the LLTO/SDC core–shell particles determined by EDX. Only Sm, Ce, La and Ti elements are included for percentage calculation

Region		Sm (%)	Ce (%)	La (%)	Ti (%)
Darker core	Particle 1	20.5	70.9	5.7	2.8
	Particle 2	21.4	70.3	4.7	3.5
	Particle 3	18.2	71.7	5.8	4.4
Brighter shell	Particle 1	3.0	2.9	43.3	50.8
	Particle 2	7.6	6.1	40.1	46.2
	Particle 3	6.3	5.3	40.4	48.0

patterns of LLTO with a tetragonal perovskite structure and SDC with a cubic fluorite structure are presented. The XRD patterns of the LLTO-infiltrated anodes are well indexed with the LLTO and SDC phases. The electrical conductivities of the various infiltrated electrodes fired at 800 and 900 °C for 2 hours were measured using the 4-probe DC method. As shown in Fig. 4b, the maximum conductivity of the LLTO infiltrated electrode calcined at 800 °C was lower than 0.2 S cm^{-1}, likely due to the isolated LLTO nanoparticles of the infiltrated electrode. For the samples calcined at 900 °C, the electrical conductivity dramatically increased to >2 S cm^{-1} at 800 °C. Thus, the formation of thin films likely contributes to promising conductivity. Thermomechanical stability is another important concern for SOFC electrode development. Large differences in the thermal expansion coefficients (TECs) of cell components may introduce large internal stress during operation, which can result in rapid degradation in cell performance due to the delimitation. A significant advantage of an infiltrated electrode is that the TEC mismatch between the electrode and the electrolyte will be small if the scaffold is made from materials that have a TEC similar to that of the electrolyte. For the infiltrated electrode, the thermal expansion behavior is similar to that of the scaffold, while the TEC of a composite electrode is a weighted average of its components. The thermal expansion curves of a porous SDC scaffold and a LLTO infiltrated SDC anode fired at 900 °C are

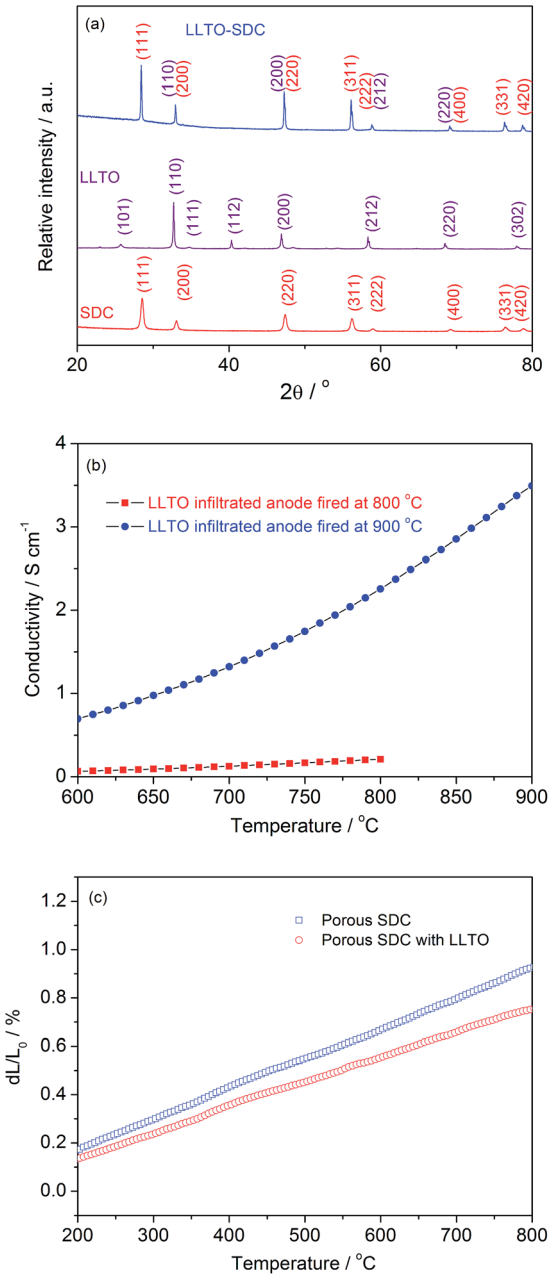

Fig. 4 (a) XRD patterns of LLTO-infiltrated SDC anodes after calcination at 900 °C for 2 hours, as well as the pure phases such as SDC and LLTO; (b) electrical conductivities of the LLTO infiltrated SDC anodes after sintering at 800 and 900 °C for 2 hours and (c) thermal expansion behaviors of the porous SDC and LLTO-infiltrated SDC bars sintered at 900 °C.

shown in Fig. 4c. The calculated TEC of porous SDC is 12.6 × 10^{-6} K^{-1} at a temperature of 200–800 °C, which matches the reported values of SDC in the literature.[28] In addition, a TEC value of 10.3 × 10^{-6} K^{-1} was calculated from the thermal expansion curve for the LLTO infiltrated SDC anode. This result suggests that the core–shell structured anode is compatible with the electrolyte. Consequently, long-term operational stability is expected. In addition, the TEC of the LLTO material has been reported to be 9.35 × 10^{-6} K^{-1} from 298 K to 800 K,[29]

while the TEC value of the SDC scaffold in this study is 11.3 × 10^{-6} K^{-1} under the same conditions, suggesting almost no thermal incompatibility between LLTO and SDC in the core–shell structure.

To test the performance of the SOFCs with the infiltrated LLTO anode for power generation, an electrolyte-supported SOFC with a LLTO/SDC|SDC|BSCF configuration was used. Fig. S1† shows a typical SEM image of a cross-section of an electrolyte-supported SOFC with a reduced LLTO-infiltrated SDC anode after firing at 900 °C. The infiltrated anode, electrolyte and the cathode had thicknesses of approximately 25, 300 and 20 μm, respectively. The cell components attached to each other well, which indicated that the anode, electrolyte and cathode had good compatibility. Typical *I–V* and *I–P* polarization curves and Electrochemical Impedance Spectroscopy (EIS) spectra of the cells with the LLTO infiltrated SDC anode with different structures (core–shell and nanoparticles) at 800 °C are shown in Fig. 5. For the H_2 fuel, no obvious differences were observed for the anodes with different structures. However, some differences in the power output were found when the fuel was switched to a 1000 ppm H_2S–H_2 gas mixture. For the anode with the core–shell structure, comparable power outputs were achieved with H_2 and 1000 ppm H_2S–H_2 fuels and a sharp decrease in the power output was observed from 215 to 123 mW cm^{-2} for the anode with nanoparticles due to its poor sulfur tolerance (potentially the agglomeration of nanoparticles), as shown in Fig. 5a. Based on the EIS results from these two anodes at 800 °C, the electrode polarization resistance of the anode with a core–shell structure was comparable when using the H_2 and 1000 ppm H_2S–H_2 fuels, while the anode with nanoparticles presented a much larger electrode polarization resistance. This result agrees with the power output results.

For comparison, the widely used $La_{0.3}Sr_{0.7}TiO_3$ (LST), $SrTiO_3$ (ST) and $BaTiO_3$ (BT) perovskite infiltrated anodes were used for cell performance tests with 1000 ppm H_2S–H_2 fuel, as shown in Fig. 6. The LLTO infiltrated anode had a slightly higher power output and a smaller electrode polarization resistance than the LST, ST and BT infiltrated anodes. These results suggest that LLTO can be used as an anode for operating SOFCs using H_2S-containing fuels.

The operational stability of the fuel cell using 1000 ppm H_2S in H_2 fuel was tested under a constant current density of 100 mA cm^{-2}. Fig. 7 shows the time-dependency of the cell voltage and the operational stability of the electrolyte-supported fuel cell with the LLTO infiltrated core–shell anode operated with 1000 ppm H_2S–H_2. The fuel cell was first stabilized under polarization at a constant current density of 100 mA cm^{-2} for 24 hours using hydrogen fuel at 800 °C. For comparison, the long-term operational behavior of the fuel cells with anodes decorated

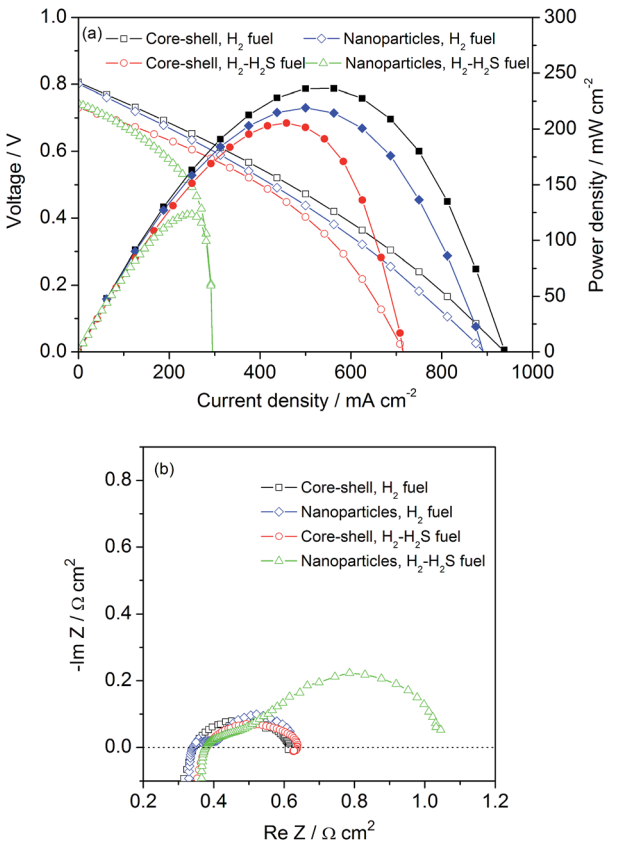

Fig. 5 The typical *I–V* and *I–P* polarization curves (a) and EIS spectra (b) of the fuel cells with LLTO-infiltrated SDC anodes with different structures operating on 1000 ppm H_2S–H_2 at 800 °C.

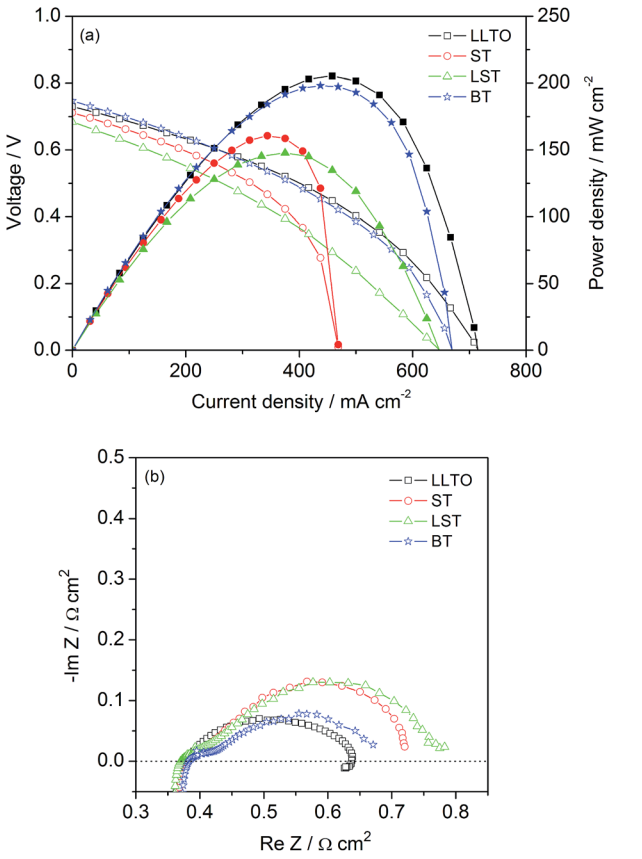

Fig. 6 Typical *I–V* and *I–P* polarization curves (a) and EIS spectra (b) of the fuel cells with different infiltrated anodes operating on 1000 ppm H_2S–H_2 at 800 °C.

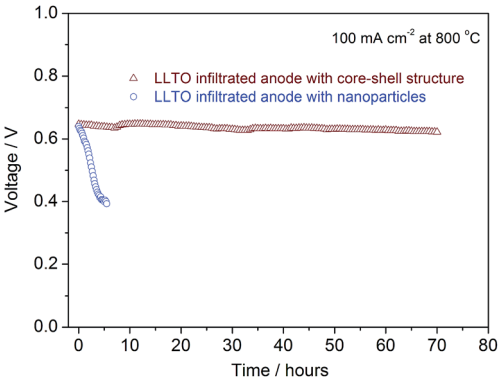

Fig. 7 Time-dependent voltage of the fuel cell with LLTO-infiltrated SDC anodes with different structures operating on 1000 ppm H_2S–H_2 under a current density of 100 mA cm^{-2} at 800 °C.

with LLTO nanoparticles was determined in the same way. The cell voltage of the fuel cell with the LLTO infiltrated core–shell anode was maintained at approximately 0.6 V over a test period of 70 hours without any obvious signs of voltage decay, featuring a stable cell performance in the electrochemical oxidation of hydrogen and H_2S. However, the LLTO anode decorated with nanoparticles was not stable and no power output was delivered after 5.5 hours' operation. The above results suggest that the core–shell LLTO infiltrated electrode can be used as a sulfur-tolerant anode for SOFCs with good operational stability. The morphologies of these two infiltrated anodes after operational stability are shown in Fig. 8. A comparison of the micrographs of the anodes operated in pure H_2 (Fig. 2) and in $H_2 + H_2S$ (Fig. 8) indicates that microstructural differences occurred in the LLTO anode decorated with nanoparticles. An agglomeration of LLTO particles from 50 nm to 200 nm was observed. However, no obvious differences were observed for the infiltrated anode fired at 900 °C. In addition, some porosity was lost due to long-term operation at high temperatures. This porosity loss explained a slight decrease in voltage during the stability test. As shown in Fig. S3,† the XRD results of the two anodes after long-term stability suggested no obvious phase change after operation using H_2S. These results further indicate that lithium-conducting LLTO is very stable in H_2–H_2S, while sulfur poisoning only results in the agglomeration of nanoparticles.

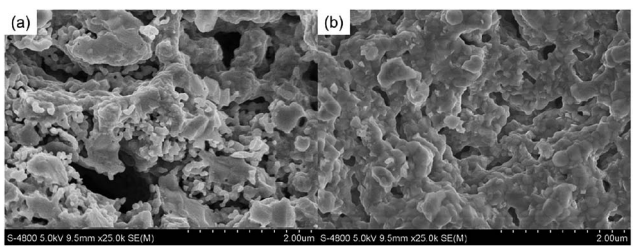

Fig. 8 SEM photos of the LLTO-infiltrated SDC anodes with different structures – (a) nanoparticles and (b) thin film – after the operational stability test on 1000 ppm H_2S–H_2 fuel.

To further improve the cell performance of the core–shell LLTO infiltrated anode, a small amount of active phase Ni was added during the infiltration stage and a core–shell structure was obtained, as evidenced by the SEM images shown in Fig. 9. Similar to the LLTO-infiltrated anode calcined at 800 °C, nanoparticles with a diameter of 50 nm were identified on the surface of the SDC scaffold (Fig. 9a). After calcination at 850 °C, the amount of nanoparticles on the SDC scaffold decreased (Fig. 9b). Furthermore, the nanoparticles disappeared following calcination at 900 and 1000 °C, implying the formation of a Ni + LLTO thin film over the SDC scaffold (Fig. 9c and d). The core–shell structure was further confirmed by the TEM results shown in Fig. S3.† The XRD and TEC results shown in Fig. S4 and S5† suggest that the successful infiltration of Ni to the SDC scaffold and the TEC of the Ni–LLTO co-infiltrated anodes were similar to those of the SDC scaffold.

The *I–V* and *I–P* polarization curves of the single cell operated using H_2 and 1000 ppm H_2S–H_2 fuels at various temperatures are shown in Fig. 10. Overall, peak power densities (PPDs) of up to 446 and 437 mW cm^{-2} were achieved for the Ni–LLTO co-infiltrated anodes at 800 °C when using H_2 and 1000 ppm H_2S–H_2 fuels, respectively. These results are highly attractive because thick electrolytes were applied in this study. Considering the thickness (300 μm) and oxygen-ion conductivity of the SDC electrolyte at 800 °C (0.1 S cm^{-1}), the PPD can reach 570 mW cm^{-2} for cells using the SDC (300 μm) electrolyte by assuming that no polarization resistance resulted from the electrodes. This result suggests that the reduced Ni–LLTO co-infiltrated anode has high hydrogen electro-oxidation activity and good sulfur tolerance. The related EIS spectra from the fuel cells operated using H_2 and 1000 ppm H_2S–H_2 fuels at various temperatures are presented in Fig. S6.† The above results suggest that the infiltrated core–shell structured composite could be used as a highly active anode material for SOFCs operating on sulfur-containing fuels. Furthermore, as shown in Fig. S7,† an initial stability of 25 hours could be obtained using a Ni–LLTO co-infiltrated anode and only a slight degradation was observed.

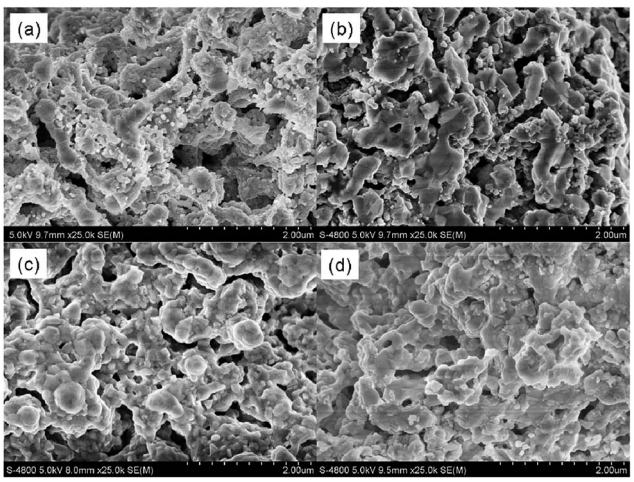

Fig. 9 SEM images of the Ni–LLTO co-infiltrated SDC anodes after firing at (a) 800, (b) 850, (c) 900 and (d) 1000 °C for 2 hours.

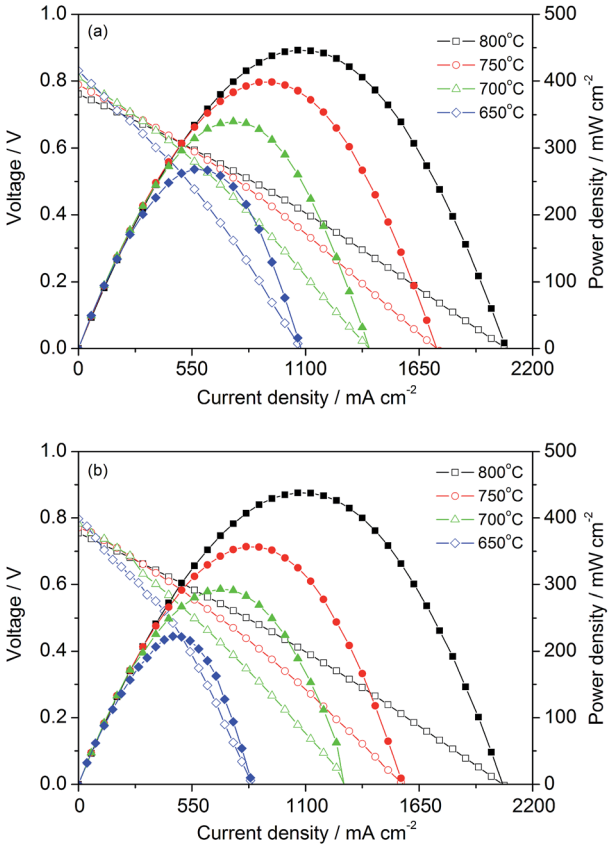

Fig. 10 The typical *I–V* and *I–P* polarization curves of the fuel cells with Ni–LLTO co-infiltrated SDC anodes after calcination at 900 °C operating on H_2 (a) and 1000 ppm H_2S–H_2 (b).

Conclusions

In conclusion, a core–shell structured anode was successfully fabricated using a simple infiltration approach. The as-prepared core–shell structured LLTO electrode was chemically and thermally compatible between components, resulting in excellent electrochemical hydrogen electro-oxidation activity and maintaining excellent operational stability for 70 hours with no obvious degradation at 800 °C in fuel cells operating on 1000 ppm H_2S–H_2. However, the LLTO infiltrated anodes with nanoparticles displayed much lower power outputs and lower operational stability under the same conditions. In addition, the Ni active phase was added to the LLTO infiltrated anodes during the infiltration stage, and the core–shell structure was obtained. A high power output of 437 mW cm^{-2} was obtained using 1000 ppm H_2S–H_2 fuel. The above results offered an effective approach for developing sulfur-tolerant electrodes for SOFCs for practical applications, which could accelerate the commercialization of SOFC technology.

Experimental section

Fuel cell fabrication

The SDC scaffold and electrolyte bi-layer were fabricated as previously reported.[26] Then, the cathode was spray-deposited onto another side surface of the prepared SDC electrolyte, which created an effective cathode area of 0.48 cm^2. Next, the cathode was fired at 1000 °C for 2 hours. The 0.6 mol L^{-1} LLTO precursor solution for infiltration was prepared by stoichiometrically mixing $La(NO_3)_3 \cdot 6H_2O$, $LiNO_3$ and $Ti(OC_4H_9)_4$ in distilled water. To obtain the aqueous solution, $Ti(OC_4H_9)_4$ was added into citric acid while heating and stirring to form lemon titanium. Then, the $La(NO_3)_3 \cdot 6H_2O$ and $LiNO_3$ were added into the aqueous solution, and citric acid was added at a molar ratio of 2 : 1 to the total amount of cations. Ethanol was used as a surfactant to improve the wettability of the solution on the SDC scaffold. The infiltration process was carried out on a hot plate (60 °C) to accelerate gas expulsion and enhance the fluidity of the solution in the porous scaffold. After each infiltration, the pellet was calcined in air at 400 °C for 30 min to decompose metal nitrates and citric acid. Multiple steps were required to reach the final loading of ~30 wt%. Next, the composite anode was calcined in air at 800, 900 or 1000 °C for 2 hours. A similar process was used to prepare the $La_{0.3}Sr_{0.7}TiO_3$ (LST), $SrTiO_3$ (ST) and $BaTiO_3$ (BT) infiltrated anodes for comparison. For the Ni-modified LLTO infiltrated anode, Ni was added at ~8 wt% after achieving ~30 wt% LLTO. Then, the resulting composite was calcined in air at 800, 850, 900 or 1000 °C for 2 hours. $Ba_{0.5}Sr_{0.5}Co_{0.8}Fe_{0.2}O_{3-\delta}$ (BSCF), $Sm_{0.5}Sr_{0.5}CoO_{3-\delta}$ (SSC) and $Sm_{0.2}Ce_{0.8}O_{1.9}$ (SDC) were synthesized using an EDTA–citrate complexing sol–gel method.[30] The precursors were further calcined in ambient air at 950 °C (BSCF), 1000 °C (SSC) and 800 °C (SDC) for 5 hours, separately, to achieve the desired crystal phase.[30]

Characterizations

The *I–V* and *I–P* curves of the fuel cells were obtained using a Keithley 2420 source meter based on a four-probe configuration. During the measurements, H_2 or 1000 ppm H_2S–H_2 fuels were fed into the anode chamber, and ambient air was used as the cathode atmosphere. The flow rate of H_2 or 1000 ppm H_2S–H_2 fuel was maintained at 80 mL min^{-1} [STP]. The resistance of the fuel cell was investigated using EIS measurements with a Solartron 1260 Frequency Response Analyzer in combination with a Solartron 1287 potentiostat. The frequency of the EIS measurements ranged from 0.1 to 1000 kHz, and the signal amplitude was 20 mV. To avoid potential CO_2 poisoning and the phase transition at the BSCF cathode during the stability test, SSC was used as a cathode material. To avoid potential degradation of the Ag paste used in the current collector, mesh-like Ag was used during the stability evaluation.[31] The phase structures of the samples were observed using an XRD (Bruker D8 Advance) with Cu Kα radiation (λ = 0.1541 nm). Powder samples were prepared for TEM, as described in our previous work.[30] The thermal expansion behavior of the anode materials in air from 200 to 800 °C was determined by using a Netzsch DIL 402C/3/G dilatometer at a heating rate of 5 °C min^{-1}. The anode morphologies were observed by using field emission scanning electron microscopy (FESEM, JEOL-S4800).

Acknowledgements

This work was supported by Project of Priority Academic Program Development of Jiangsu Higher Education Institutions.

Notes and references

1 V. Vorontsov, J. L. Luo, A. R. Sanger and K. T. Chuang, *J. Power Sources*, 2008, **183**, 76–83.
2 J. Ober, *US Geological Survey Minerals Yearbook, Sulfur*, US Geological Survey, 2004, pp. 74.1–74.18.
3 A. Piéplu, O. Saur, J. Lavalley, O. Legendre and C. Nédez, *Catal. Rev.: Sci. Eng.*, 1998, **40**, 409–450.
4 C. Yang, Z. Yang, C. Jin, G. Xiao, F. Chen and M. Han, *Adv. Mater.*, 2012, **24**, 1439–1443.
5 L. Yang, Z. Cheng, M. Liu and L. Wilson, *Energy Environ. Sci.*, 2010, **3**, 1804–1809.
6 Z. Cheng, J. Wang, Y. Choi, L. Yang, M. C. Lin and M. Liu, *Energy Environ. Sci.*, 2011, **4**, 4380–4409.
7 W. Wang, C. Su, Y. Z. Wu, R. Ran and Z. P. Shao, *Chem. Rev.*, 2013, **113**, 8104–8151.
8 F. Wang, W. Wang, J. F. Qu, Y. J. Zhong, M. O. Tade and Z. P. Shao, *Environ. Sci. Technol.*, 2014, **48**, 12427–12434.
9 N. U. Pujare, K. W. Semkow and A. F. Sommells, *J. Electrochem. Soc.*, 1987, **134**, 2639–2640.
10 A. Hagen, J. F. B. Rasmussen and K. Thydén, *J. Power Sources*, 2011, **196**, 7271–7276.
11 Y. Matsuzaki and I. Yasuda, *Solid State Ionics*, 2000, **132**, 261–269.
12 K. Sasaki, K. Susuki, A. Iyoshi, M. Uchimura, N. Imamura, H. Kusaba, Y. Teraoka, H. Fuchino, K. Tsujimoto, Y. Uchida and N. Jingo, *J. Electrochem. Soc.*, 2006, **153**, A2023–A2029.
13 C. Xu, J. W. Zondlo, M. Gong, F. Elizalde-Blancas, X. Liu and I. B. Celik, *J. Power Sources*, 2010, **195**, 4583–4592.
14 Z. Cheng, S. Zha, L. Aguilar, D. Wang, J. Winnick and M. L. Liu, *Electrochem. Solid-State Lett.*, 2006, **9**, A31–A33.
15 Y. H. Huang, R. I. Dass, Z. L. Xing and J. B. Goodenough, *Science*, 2006, **312**, 254–257.
16 N. Danilovic, J.-L. Luo, K. T. Chuang and A. R. Sanger, *J. Power Sources*, 2009, **192**, 247–257.
17 C. Peng, J. Luo, A. R. Sanger and K. T. Chuang, *Chem. Mater.*, 2010, **22**, 1032–1037.
18 L. Yang, S. Wang, K. Blinn, M. Liu, Z. Liu, Z. Cheng and M. L. Liu, *Science*, 2009, **326**, 126–129.
19 S. Zha, P. Tsang, Z. Cheng and M. L. Liu, *J. Solid State Chem.*, 2005, **178**, 1844–1850.
20 Y. Bu, Q. Zhong, D. Xu and W. Tan, *J. Alloys Compd.*, 2013, **578**, 60–66.
21 Y.-F. Bu, Q. Zhong, D.-D. Xu, X.-L. Zhao and W.-Y. Tan, *J. Power Sources*, 2014, **250**, 143–151.
22 J.-H. Li, X.-Z. Fu, J.-L. Luo, K. T. Chuang and A. R. Sanger, *J. Power Sources*, 2012, **213**, 69–77.
23 A. Torabi and T. H. Etsell, *J. Power Sources*, 2013, **225**, 51–59.
24 S.-H. Cui, J.-H. Li, X.-W. Zhou, G.-Y. Wang, J.-L. Luo, K. T. Chuang, Y. Bai and L.-J. Qiao, *J. Mater. Chem. A*, 2013, **1**, 9689–9696.
25 A. Vincent, J.-L. Luo, K. T. Chuang and A. R. Sanger, *J. Power Sources*, 2010, **195**, 769–774.
26 D. J. Chen, G. M. Yang, F. Ciucci, M. O. Tadé and Z. P. Shao, *J. Mater. Chem. A*, 2014, **2**, 1284–1293.
27 D. Ding, X. Li, S. Y. Lai, K. Gerdes and M. L. Liu, *Energy Environ. Sci.*, 2014, **7**, 552–575.
28 E. Y. Pikalova, V. I. Maragou, A. N. Demina, A. K. Demin and P. E. Tsiakaras, *J. Power Sources*, 2008, **181**, 199–206.
29 T. Okumura, A. Dodomi, M. Saito and J. Kuwano, *Key Eng. Mater.*, 2006, **320**, 275–278.
30 W. Wang, C. Su, R. Ran, B. T. Zhao, Z. P. Shao, M. O. Tade and S. M. Liu, *ChemSusChem*, 2014, **7**, 1719–1728.
31 Y. Chen, F. Wang, D. Chen, F. Dong, H. J. Park, C. Kwak and Z. P. Shao, *J. Power Sources*, 2012, **210**, 146–153.